Few- to many-vortex states of density-angular-momentum–coupled Bose-Einstein condensates

Matthew Edmonds◉

Department of Physics and Research and Education Center for Natural Sciences, Keio University,
Hiyoshi 4-1-1, Yokohama, Kanagawa 223-8521, Japan

Motivated by recent experiments, we study theoretically a gas of atomic bosons confined in an elliptical harmonic trap, forming a quasi-two-dimensional atomic Bose-Einstein condensate subject to a density-dependent gauge potential which realizes an effective density-angular-momentum coupling. We present exact Thomas-Fermi solutions which allow us to identify the stable regimes of the full parameter space of the model. Accompanying numerical simulations reveal the effect of the interplay of the rigid body and density-angular-momentum coupling for the elliptically confined condensate. By varying the strength of the gauge potential and trap anisotropy, we explore how the superfluid state emerges in different experimentally accessible geometries, while for large rotation strengths dense vortex lattices and concentric vortex ring arrangements are obtained.

DOI: 10.1103/PhysRevA.104.043310

I. INTRODUCTION

Quantum and classical fluids can respond to rotation by the nucleation of vortices, effective holes in the fluid density around which there exists a net circulation. While classical fluids manifest vortices for arbitrary rotation, vortices in quantum fluids appear instead when a *minimum* rotation is met and are unique since their allowed rotational properties are restricted. Early experimental work demonstrated the feasibility of generating quantum vortices in equilibrium atomic gases [1–4], while ongoing work has explored nonequilibrium effects such as quantum turbulence [5], the Berezinskii-Kosterlitz-Thouless transition [6], Kibble-Zurek dynamics [7], and the emergence of equilibrium [8] and ordered states [9].

Degenerate quantum gases represent a powerful tool for investigating the phenomenology of analog systems such as the quantum simulation of effects drawn from condensed matter [10], quantum information and computing [11], and metrological applications [12]. Atomic gases benefit from being highly controllable; here the statistics, particle interactions, dimensionality, and potential landscape can be engineered with high fidelity to realize novel and exotic states of quantum matter [13] such as the recent experimental progress with topological phenomena [14,15] with these systems.

Quantum vortices represent the fundamental excitations of superconductors and superfluids alike, appearing in response to magnetic or rotational driving, respectively. Although the atomic superfluids He II and weakly interacting Bose-Einstein condensates both nucleate vortices, the condensate fraction of He II is small ($\sim$10%) in comparison to that of atomic condensates which typically contain only a very small fraction of noncondensate atoms. While studying vortex physics with strongly interacting superfluids such as He II is challenging, the weakly correlated quantum fluids have shown to be strong candidates for understanding superfluid vortices and their

dynamics. Experiments have generated vortex dipoles [16], observed individual vortex dynamics [17], created vortices through interference techniques [18], and realized multiply quantized vortices [19,20]. Theoretical interest in these systems has focused on understanding the fundamental properties of the superfluid state [21], anisotropic trapping [22–27], coherent couplings [28–31], and the dynamics and ordering properties of few- [32] and many-vortex states [33,34].

Parallel to these developments, neutral ultracold quantum gases have become a prominent platform for the generation of synthetic forms of matter. Artificial gauge potentials represent a burgeoning subdiscipline of this field [35,36], where experiments have demonstrated orbital magnetism [37–39] and spin-orbit [40] and spin-angular-momentum couplings with bosons [41–43] and fermions [44,45]. These experiments are based on versatile Raman techniques [46] that allow the internal states of atomic gases to be optically dressed to mimic the mathematical structure of a variety of gauge theories [47]. The versatile toolbox of quantum technologies now allows for the creation of gauge potentials giving rise to spatially varying synthetic magnetic fields which have been shown to lead to unusual manifestations of superfluidity with a single component [48], spin-orbit-coupled systems [49], and proposals for atom-surface mediated gauge theories [50–52].

All the gauge potentials realized in this way, however, are static; there is no feedback between the light and the matter field. To address this, there is a growing subfield whose aim instead is to simulate *dynamical* [53–55] gauge potentials. One methodology to overcome this problem is to directly couple the gauge potential and the quantum state of the system, which naturally introduces a time-dependent feedback in the form of a *density-dependent* gauge potential either in the continuum [56] or for lattice-based theories [57–60]. The associated phenomenology has revealed a wealth of unusual effects; in the one-dimensional context the theory violates Kohn's theorem [61,62] and possesses exact chiral soliton solutions

[63–67], as well as exhibiting unusual transport effects when confined in double-well [68] or harmonic potentials [69]. The rotational properties of the theory present an opportunity to understand the vortex solutions and associated superfluidity in two-dimensional homogeneous [70,71] and trapped configurations [72], as well as the simulation of curved space-time for the excitations of the ground state [73]. Recent work has also examined the theory's mathematical structure from a hydrodynamical perspective [74,75], and proposals have now appeared that generalize the theory to support gauge theories such as those with a topological Chern-Simons structure [76], as well as density-dependent spin-orbit coupling [77].

Complementary to its theoretical appeal, density-dependent magnetism has also been demonstrated experimentally with bosons [78] and fermions [79] confined in two-dimensional optical lattices as well as for an ensemble of Rydberg atoms [80]. Very recently the first experiment in the continuum has also appeared realizing domain walls coupled to a density-dependent gauge potential [81]. In this work we comprehensively examine the unusual phenomenology provided by this system in a quasi-two-dimensional harmonically confined configuration, in particular focusing on the interplay of elliptical harmonic confinement and the density-dependent gauge field that manifests as a density-angular-momentum coupling, using a combination of analytical and numerical approaches to identify unconventional phenomena in experimentally accessible regimes.

The paper is organized as follows. In Sec. II we derive the density-dependent gauge theory and particularize the model such that the gauge potential manifests as a density-angular-momentum coupling of the atomic cloud in the quasi-two-dimensional limit. We then derive the static (Thomas-Fermi) solutions to this model, which we use to explore the stable regions of the total parameter space of the model, as well as discussing the requirements for a future experiment. Following this we present in Sec. III detailed calculations of the vortical stationary states, under cylindrical and general elliptical harmonic confinement. We also explore the effect of the nonlinear rotation on the formation of vortex lattices and rings comprised of larger numbers of vortices. We summarize in Sec. IV.

II. THEORETICAL MODEL

A. Density-dependent gauge theory

In what follows we demonstrate how to construct a density-dependent gauge theory using a weakly interacting two-component atomic Bose gas. This is based on the adiabatic theorem, where the gauge potentials appear as geometric vector and scaler potentials. Our system comprises N two-level atoms coupled via a coherent light-matter interaction, forming a Bose-Einstein condensate. Within the rotating-wave approximation the Hamiltonian can be written as

$$\hat{H} = \left[\frac{\hat{\mathbf{p}}^2}{2m} + V(\mathbf{r}) \right] \otimes \mathbb{1} + \hat{H}_{\text{int}}(\mathbf{r}) + \hat{\mathcal{U}}_{\text{MF}}, \quad (1)$$

where the light-matter interaction is defined as

$$\hat{\mathcal{U}}_{\text{MF}} = \frac{\hbar\Omega_r}{2} \begin{bmatrix} \cos\theta & e^{-i\phi}\sin\theta \\ e^{i\phi}\sin\theta & -\cos\theta \end{bmatrix}. \quad (2)$$

Here Ω_r gives the strength of the light-matter coupling and θ and ϕ are in general spatially varying quantities. While the off-diagonal components of Eq. (2) define the coherent coupling between the light and the matter, the diagonal terms define the detuning between the frequency of the driving laser ω_r and the atomic transition frequency $\omega_t = \omega_2 - \omega_1$ between the ground and excited states such that $\Delta = \omega_t - \omega_r$. Then one has $\Delta = \Omega_r \cos\theta$. The other quantities that appear in Eq. (1) are the two-body mean-field interactions $\hat{H}_{\text{int}} = \frac{1}{2}\text{diag}[\Delta_1, \Delta_2]$, with $\Delta_j = g_{jj}n_j + g_{jk}n_k$ and $g_{jk} = 4\pi\hbar^2 a_{jk}/m$ defining the scattering parameter for atoms in internal states j and k. The population density of state j is $n_j = |\psi_j|^2$ and the external harmonic confinement is provided by $V(\mathbf{r}) = m(\omega_x^2 x^2 + \omega_y^2 y^2 + \omega_z^2 z^2)/2$, where ω_j defines the trapping strength in each coordinate direction. To derive the density-dependent gauge theory, we require the eigenstates of the light-matter interaction (2), which for a two-level atom with internal states $|1, 2\rangle$ are defined

$$|+\rangle = \cos\frac{\theta}{2}|1\rangle + e^{i\phi}\sin\frac{\theta}{2}|2\rangle, \quad (3a)$$

$$|-\rangle = -e^{-i\phi}\sin\frac{\theta}{2}|1\rangle + \cos\frac{\theta}{2}|2\rangle, \quad (3b)$$

which obey $\hat{\mathcal{U}}_{\text{MF}}|\pm\rangle = \pm\hbar\Omega_r|\pm\rangle/2$. In order to construct the density-dependent gauge theory, we use perturbation theory and Eqs. (3) to build *perturbed dressed states*. Since the motion of the atoms in the dressed states must be adiabatic, this requires that $\hbar\Omega_r \gg E_R$, with $E_R = p_R^2/2m$ and $p_R = \hbar k$ giving the respective atomic recoil energy and momentum [82]. Then the alkaline-earth atoms represent a good candidate since these atoms are used for atomic metrology and in particular atomic clocks and as such possess excited states whose lifetimes are of the order of seconds [83]. The perturbed interacting dressed basis states are defined in turn as

$$|\psi_\pm\rangle = |\pm\rangle \pm \frac{\Delta_d}{\hbar\Omega_r}|\mp\rangle. \quad (4)$$

The mean-field dressed detuning appearing in Eq. (4) is defined as $\Delta_d = \langle\pm|\hat{\mathcal{U}}_{\text{MF}}|\mp\rangle = \sin\frac{\theta}{2}\cos\frac{\theta}{2}(\Delta_1 - \Delta_2)/2$. In order to derive a density-dependent gauge theory, we use the perturbed dressed states (4) to define a state $|\chi\rangle = \sum_{j=+,-} \Psi_j(\mathbf{r}, t)|\psi_j\rangle$ along with Eq. (1), and since the qualitative details of the resulting physics do not depend on which of the two dressed states we choose to project into, the atomic motion will be projected into the $|\psi_+\rangle$ state. Hence the effective Hamiltonian is written

$$\hat{H}_+ = \frac{(\mathbf{p} - \mathbf{A}_+)^2}{2m} + W_+ + \frac{\hbar\Omega_r}{2} + \Delta_+ + V(\mathbf{r}), \quad (5)$$

where the dressed mean-field atomic interactions are written as $\Delta_+ = \langle+|\hat{\mathcal{U}}_{\text{MF}}|+\rangle = (\Delta_1 \cos^2\frac{\theta}{2} + \Delta_2 \sin^2\frac{\theta}{2})/2$, while the two arising geometric potentials are consequences of the adiabatic atomic motion. The vector potential is defined by $\mathbf{A}_+ = i\hbar\langle\psi_+|\nabla\psi_+\rangle$, while the scalar potential is

$W_+ = \hbar^2 |\langle \psi_+ | \nabla \psi_- \rangle|^2 / 2m$. For atomic motion in the $|\psi_+\rangle$ state these two geometric potentials are

$$\mathbf{A}_+ = -\frac{\hbar}{2}(1 - \cos\theta)\nabla\phi + \frac{\Delta_d}{\Omega_r}\nabla\phi\sin\theta, \tag{6a}$$

$$W_+ = \frac{\hbar^2}{8m}(\nabla\theta)^2 + \frac{\hbar^2}{8m}\sin^2\theta(\nabla\phi)^2$$
$$+ \frac{\hbar}{2m}\frac{\Delta_d}{\Omega_r}\sin\theta\cos\theta(\nabla\phi)^2 - \hbar\nabla\theta\cdot\nabla\frac{\Delta_d}{\Omega_r}. \tag{6b}$$

In order to derive a mean-field equation of motion for the atoms, we write the Dirac-Frenkel action $\mathcal{S}$ as

$$\mathcal{S}[\Psi_+^*, \Psi_+] = \int dt \int d\mathbf{r}\, \Psi_+^*(\mathbf{r}, t)\left[i\hbar\frac{\partial}{\partial t} - \hat{H}_+\right]\Psi_+(\mathbf{r}, t), \tag{7}$$

which can in turn be extremized by computing $\delta\mathcal{S}/\delta\Psi_+^* = 0$, from which we obtain the generalized Gross-Pitaevskii equation [56,84]

$$i\hbar\frac{\partial}{\partial t}\Psi_+ = \left[\frac{(\mathbf{p} - \mathbf{A}_+)^2}{2m} + W_+ + \mathbf{a}_1 \cdot \mathbf{j} + \frac{\hbar\Omega_r}{2}\right.$$
$$+ 2\Delta_+ + V(\mathbf{r})\bigg]\Psi_+ + \left[n_+\left(\frac{\partial W_+}{\partial\Psi_+^*}\right.\right.$$
$$\left.\left. - \nabla\cdot\frac{\partial W_+}{\partial\nabla\Psi_+^*}\right) - \frac{\partial W_+}{\partial\nabla\Psi_+^*}\cdot\nabla n_+\right] \tag{8}$$

for atomic motion in the $|\psi_+\rangle$ dressed state. Here the strength of coupling to the gauge potential is $\mathbf{a}_1 = \nabla\phi\Delta_d\sin\theta/n_+\Omega_r$. The generalized Gross-Pitaevskii equation (8) includes a number of additional terms arising from the density dependence of the geometric potentials (6a) and (6b), in particular the current nonlinearity

$$\mathbf{j} = \frac{\hbar}{2mi}\left[\Psi_+\left(\nabla + \frac{i}{\hbar}\mathbf{A}_+\right)\Psi_+^* - \Psi_+^*\left(\nabla - \frac{i}{\hbar}\mathbf{A}_+\right)\Psi_+\right]. \tag{9}$$

The theory supports two small parameters: $\theta = \Omega_r/\Delta$, which gives the ratio of the Rabi frequency to the detuning, and $\varepsilon = n(g_{11} - g_{22})/4\hbar\Delta$, which underpins the collisional and coherent interactions. Since both of these parameters are assumed to be small, we can expand Eqs. (6a) and (6b) to first order in ε and θ, which gives the simplified relations for the vector potential

$$\mathbf{A}_+ = -\frac{\hbar\theta^2}{4}[1 - 4\varepsilon] \tag{10}$$

and the scalar potential

$$W_+ = \frac{\hbar^2}{2}\left[\frac{(\nabla\theta)^2[1 - 4\varepsilon] + \theta^2(\nabla\phi)^2[1 + 4\varepsilon]}{4m} - \nabla\theta^2\cdot\nabla\varepsilon\right], \tag{11}$$

which together with Eqs. (8) and (9) can then be used to construct a simplified density-dependent gauge theory, where the equation of motion for the condensate becomes

$$i\hbar\frac{\partial\psi}{\partial t} = \left[-\frac{\hbar^2}{2m}\nabla^2 + V(\mathbf{r}) - \Omega(\mathbf{r}, t)\hat{L}_z + g_{\text{eff}}n\right]\psi. \tag{12}$$

Equation (12) defines a type of generalized nonlinear Schrödinger equation where the condensate experiences a *nonlinear* as well as rigid-body rotation through the density-dependent rotation frequency $\Omega(\mathbf{r}, t) = \Omega + \mathcal{C}n(\mathbf{r}, t)$. The two geometric potentials θ and ϕ are given by $\theta = \theta_0\rho$ and $\phi = \varphi$, respectively, where θ_0 is a constant of proportionality arising from assuming the angle θ is small. Then the effective strength of the nonlinear rotation is $\mathcal{C} = \theta_0^2(g_{11} - g_{22})/2m\Omega_r$, while $g_{\text{eff}} = g_{11} + \hbar\theta_0^2(g_{11} - g_{22})/m\Omega_r$ defines the effective two-body scattering parameter. Finally, the angular momentum operator is given by $\hat{L}_z = \boldsymbol{\rho}\times\mathbf{p}$. In what follows we specialize to quasi-two-dimensional harmonic confinement so that the atomic cloud adopts a pancake geometry with $\omega_z \gg \omega_{x,y}$. This in turn permits us to write the full three-dimensional mean-field wave function in the factorized form $\psi(\mathbf{r}, t) = \psi(x, y, t)\exp(-z^2/2a_z^2)/\sqrt[4]{\pi a_z^2}$, which can be combined with Eq. (12) to project out the dynamics of the z coordinate. This causes the effective strengths of the two nonlinear terms g_{eff} and $\mathcal{C}$ to be scaled by the factor $1/\sqrt{2\pi}a_z$, which in what follows will be absorbed into the definitions of these two parameters for notational convenience.

B. Experimental considerations

Given the active experimental interest in these types of synthetic gauge theories [78–81], let us outline the key ingredients required to realize the density-angular-momentum–coupled gauge theory (12). The geometric phase methodology on which the model is based is generated by the light-matter interaction (2). Laser light possessing fixed angular momentum can be exploited in order to generate the required mathematical structure of the gauge theory [85]. The recent experiments demonstrating spin-angular-momentum–coupled Bose-Einstein condensates used Laguerre-Gaussian laser light with a radially varying electric-field profile [41–43]

$$\mathcal{E}(\mathbf{r}) = \mathcal{E}_0 e^{-i\ell\varphi}\left(\frac{\rho}{w}\right)^{|\ell|} e^{-\rho^2/w^2} e^{ikz}, \tag{13}$$

where $\mathcal{E}_0$ is the amplitude, w is waist of the beam, and k is the wave number. For $\ell = 1$, Eq. (13) has precisely the spatial structure that is required since $\phi = \varphi$ and $\theta \propto \rho$. Accompanying these requirements, the perturbative requirement must also be satisfied such that $\varepsilon \ll 1$, and since ε directly depends on the difference of scattering lengths $g_{11} - g_{22}$ [see Eq. (10)], optical Feshbach resonances for alkaline-earth atoms represent an important resource for tuning this parameter [86].

C. Static solutions and stability analysis

The energy functional associated with Eq. (12) can be written in a hydrodynamic picture described by the density $n(\rho, \varphi)$ and phase $\vartheta(\rho, \varphi)$ degrees of freedom, where ρ and φ define the polar coordinates using the Madelung decomposition $\psi(\rho, \varphi) = \sqrt{n(\rho, \varphi)}\exp[i\vartheta(\rho, \varphi)]$ as

$$E[n, \vartheta] = \int d\boldsymbol{\rho}\, n\left[\frac{\hbar^2}{2m}\frac{|\nabla n|^2}{4n^2} + \frac{m}{2}\mathbf{v}^2 + \frac{i\hbar}{2mn}\nabla n\cdot\mathcal{A}\right.$$
$$\left. - \frac{\mathcal{A}^2}{2m} + V(\rho) + \frac{g_{\text{eff}}n}{2} - \mu'\right], \tag{14}$$

where $\mathbf{v} = (\hbar\nabla\vartheta - \mathcal{A})/m$ defines the hydrodynamic kinetic velocity, while $\mathcal{A} = m\boldsymbol{\Omega}\times\boldsymbol{\rho}$ and $\boldsymbol{\Omega} = \hat{e}_z(\Omega + \mathcal{C}n/2)$. Working

in the limit $g_{\text{eff}} N/\hbar\omega_x a_x^2 \gg 1$ allows us to drop the quantum pressure term appearing in Eq. (14). Then, by first minimizing the energy functional (14) with respect to the hydrodynamic phase $\vartheta(\rho, t)$, the superfluid velocity $\mathbf{v}_{\text{sf}} = \mathbf{\Omega} \times \rho$ is obtained. Subsequently inserting $\mathbf{v}_{\text{sf}}$ into Eq. (14) and then minimizing with respect to the hydrodynamic density $n(\rho, \varphi)$, we obtain the rotating frame Thomas-Fermi distribution

$$V(\rho) - \frac{m}{2}\rho^2\left(\Omega^2 + 2\Omega\mathcal{C}n + \frac{3}{4}\mathcal{C}^2 n^2\right) + g_{\text{eff}}n = \mu', \quad (15)$$

where $\rho^2 = x^2 + y^2$, the elliptical harmonic trap is $V(\rho) = \frac{1}{2}m(\omega_x^2 x^2 + \omega_y^2 y^2)$, μ' is the chemical potential in the rotating frame, and the Cartesian boundaries of the cloud are found from $R_{x,y}^2 = 2\mu'/m(\omega_{x,y}^2 - \Omega^2)$. In the limit $\mathcal{C} \to 0$ we recover the standard rotating frame Thomas-Fermi distribution

with $n(\rho) = \{\mu' - [V(\rho) - \frac{1}{2}m\Omega^2\rho^2]\}/g_{\text{eff}}$. By imposing the normalization condition

$$\int d\rho\,\theta(\mu' - V(\rho))n(\rho) = N, \quad (16)$$

in this limit we obtain

$$\mu' = \sqrt{\frac{mg_{\text{eff}}N}{\pi}}\sqrt[4]{(\omega_x^2 - \Omega^2)(\omega_y^2 - \Omega^2)}, \quad (17)$$

which defines the corresponding chemical potential, which can be shown to possess real ($\mu' > 0$) solutions when $\Omega < \omega_y$ and $\Omega < \omega_x$. The two trapping frequencies $\omega_{x,y}$ define the maximum rigid-body rotation strength. Equation (15) is quadratic in the density distribution $n(\rho, \varphi)$ and can be solved straightforwardly to give

$$n(x, y) = -\frac{4}{3m\mathcal{C}^2\rho^2}\left\{-[g_{\text{eff}} - m\Omega\mathcal{C}\rho^2] + \sqrt{[g_{\text{eff}} - m\Omega\mathcal{C}\rho^2]^2 + \frac{3m\mathcal{C}^2\rho^2}{2}\left\{\frac{1}{2}m([\omega_x^2 - \Omega^2]x^2 + [\omega_y^2 - \Omega^2]y^2) - \mu'\right\}}\right\}. \quad (18)$$

Equation (18) gives in general the shape of the background of the trapped condensate under both nonlinear and rigid-body rotation. Here we will consider the limit $\Omega = 0$, which corresponds to a vortex-free state and allows us to construct semianalytic and analytical solutions. The solutions in general are bounded by the ellipse $R_x^2(\omega_x^2 - \Omega^2) + R_y^2(\omega_y^2 - \Omega^2) = 2\mu'/m$. The normalization integral (16) can then be partially evaluated by switching to polar coordinates and leads to the expression

$$\sinh^{-1}\sqrt{\frac{\omega_x^2(1 - \alpha^2)}{\omega_y^2 - \omega_x^2}} - \sinh^{-1}\sqrt{\frac{\omega_x^2}{\omega_y^2 - \omega_x^2}}$$
$$+ \int_0^{2\pi}\frac{d\varphi}{2\pi}\frac{\omega_x\alpha}{\sqrt{\omega_x^2 + [\omega_y^2 - \omega_x^2]\sin^2\varphi}}$$
$$\times \tanh^{-1}\left[\frac{\omega_x\alpha}{\sqrt{\omega_x^2 + [\omega_y^2 - \omega_x^2]\sin^2\varphi}}\right]$$
$$= \frac{3m\mathcal{C}^2 N}{8\pi g_{\text{eff}}}, \quad (19)$$

where for brevity we have defined the dimensionless ratio $\alpha = \sqrt{3}\mathcal{C}\mu'/2\omega_x g_{\text{eff}}$ which connects the chemical potential μ', nonlinear rotation strength $\mathcal{C}$, and quasi-two-dimensional scattering parameter g_{eff}. The final angular integration appearing in Eq. (19) cannot in general be reduced to an elementary function, except for the special case of when the trap has cylindrical symmetry so $\omega_y = \omega_x$. This leads to the expression

$$\ln\left[1 - \frac{3\mathcal{C}^2\mu'^2}{4\omega_x^2 g_{\text{eff}}^2}\right] + \frac{\sqrt{3}\mathcal{C}\mu'}{\omega_x g_{\text{eff}}}\tanh^{-1}\left[\frac{\sqrt{3}\mathcal{C}\mu'}{2\omega_x g_{\text{eff}}}\right] = \frac{3m\mathcal{C}^2 N}{4\pi g_{\text{eff}}}. \quad (20)$$

Equation (20) defines an implicit relationship between the chemical potential and the various interaction parameters, whose logarithmic nature means that the allowed solutions exist on the finite domain $-2\omega_x g_{\text{eff}}/\sqrt{3}\mu' \leqslant \mathcal{C} \leqslant$

$2\omega_x g_{\text{eff}}/\sqrt{3}\mu'$. From this we can identify a minimum value of the chemical potential $\mu'_{\text{min}} = 2\omega_x g_{\text{eff}}/\sqrt{3}\mathcal{C}_{\text{max}}$, which using Eq. (20) in turn allows us to obtain the maximum nonlinear rotation strength $\mathcal{C}_{\text{max}}$ as

$$\mathcal{C}_{\text{max}} = \sqrt{\frac{8\pi\ln 2}{3}\frac{g_{\text{eff}}}{Nm}}, \quad (21)$$

which for $\mathcal{C} > \mathcal{C}_{\text{max}}$ (or $\mathcal{C} < -\mathcal{C}_{\text{max}}$) means the nonlinear rotation overcomes the harmonic confinement and the condensate no longer exists, a situation analogous to the case of pure ($\mathcal{C} = 0$) rigid-body rotation when the trapped gas is rotated faster than the harmonic trapping strength such that $\Omega > \omega_{x,y}$ [viz., Eq. (17)]. Using Eq. (21), we obtain the corresponding minimum chemical potential as

$$\mu'_{\text{min}} = \sqrt{\frac{N}{\pi\ln 4}m\omega_x^2 g_{\text{eff}}}. \quad (22)$$

Since the chemical potential can be related to the total energy via the standard thermodynamic relation $\mu'_{\text{min}} = \partial E_{\text{min}}/\partial N$, Eq. (22) yields the relation $E_{\text{min}} = \frac{2}{3}N\mu'_{\text{min}}$. Then, using the definition $R_{\text{TF}}^2 = 2\mu'_{\text{min}}/m\omega_x^2$, we obtain the Thomas-Fermi length scale associated with Eqs. (21) and (22),

$$R_{\text{TF}} = \left(\frac{2}{\pi\ln 2}\frac{g_{\text{eff}}N}{m\omega_x^2}\right)^{1/4}. \quad (23)$$

Knowledge of the chemical potential given by Eq. (22) and intrinsic length scale (23) provides useful insight for potential future experimental studies, since these points in the parameter space show predominantly the effect of the nonlinear rotation as well as providing key information about the stable regions of the total parameter space of the model. In general, for elliptical harmonic confinement ($\omega_y \neq \omega_x$) Eq. (19) can be solved numerically to understand the regions where the condensate exists and as such the maximum nonlinear rotation strength for the cylindrically symmetry [Eq. (21)] provides a useful reference point to understand the more general elliptical case ($\omega_y \neq \omega_x$).
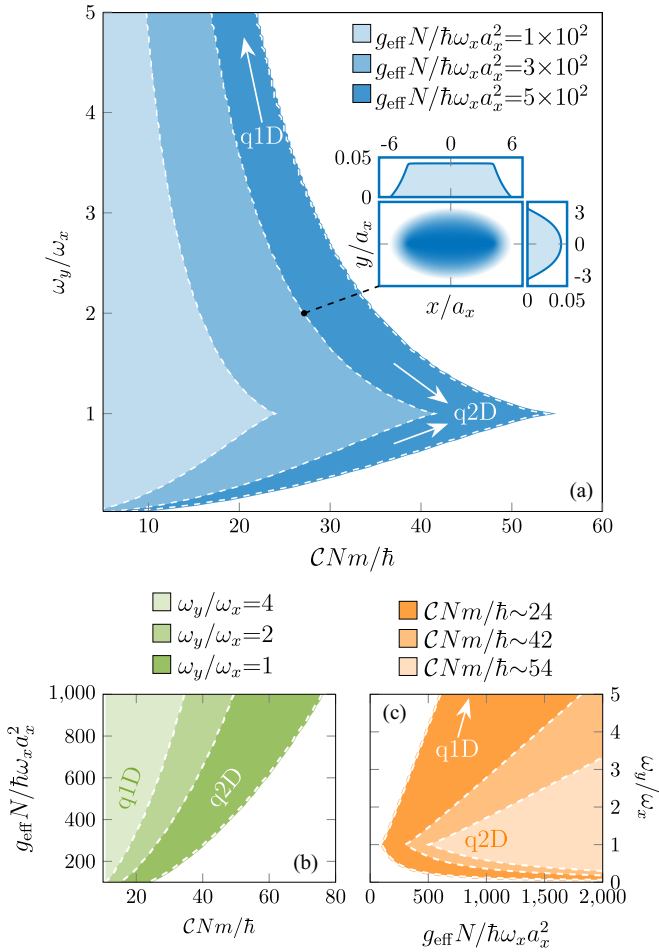
FIG. 1. Nonlinear rotation stability. (a) Boundaries (maximum nonlinear rotation strength $\mathcal{C}$) for various fixed interaction strengths g_{eff} in the ω_y/ω_x and $\mathcal{C}$ parameter space, along with an example inset density profile $|\psi|^2$ for ($\mathcal{C}Nm/\hbar\sim27$, $\omega_y/\omega_x = 2$). Also shown are the counterparts of (a) except with fixed (b) trap ellipticity and (c) nonlinear rotation strength.

Figure 1 shows the numerical solutions obtained from Eq. (19) in the parameter space of the trap anisotropy ω_y/ω_x, nonlinear rotation strength $\mathcal{C}Nm/\hbar$, and two-body mean-field interaction strength $g_{\text{eff}}N/\hbar\omega_x a_x^2$. The allowed solutions are presented in the (ω_y/ω_x, $\mathcal{C}Nm/\hbar$) parameter space in Fig. 1(a). Here each of the three shaded regions corresponds to the allowed solutions for a particular fixed value of the two-body mean-field strength $g_{\text{eff}}N/\hbar\omega_x a_x^2 = 1 \times 10^2, 3 \times 10^2, 5 \times 10^2$. The dotted white boundaries in each case represent the maximum value of the nonlinear rotation strength $\mathcal{C}Nm/\hbar$ at which a solution can be obtained for the Thomas-Fermi density (18). The accompanying inset shows an example solution for $|\psi|^2$, for $g_{\text{eff}}N/\hbar\omega_x a_x^2 = 3 \times 10^2$ with trap anisotropy $\omega_y/\omega_x = 2$. The two panels above and below this show cross sections of $|\psi(x, y = 0)|^2$ and $|\psi(x = 0, y)|^2$, respectively. The density cut along $y = 0$ reveals the effect of the density-angular-momentum coupling, giving a flattened top to the density profile, similar to a quantum droplet [87]. Figures 1(b) and 1(c) depict the allowed solutions for fixed trap anisotropy [Fig. 1(b)] and fixed nonlinear rotation

strength [Fig. 1(c)]. Note that the white-dashed boundaries shown in Fig. 1(c) depict the minimum value of the two-body mean-field interaction g_{eff} at which a solution to Eqs. (18) and (19) can be obtained. For the case of cylindrical symmetry, this minimum can be shown to be

$$g_{\text{eff}}^{\min} = \frac{3}{8\pi \ln 2}\mathcal{C}^2 Nm. \tag{24}$$

In Figs. 1(a)–1(c) the quasi-two- and quasi-one-dimensional regions are annotated with accompanying arrows. The addition of the nonlinear rotation means we must also consider the effect of the parameter $\mathcal{C}$ on the validity of the Thomas-Fermi approximation. Since we work in a perturbative regime $\Delta_d \ll \hbar\Omega_r$, the effect of the gauge field might either be negligible or require very large coupling strengths to have any effect that would in turn violate perturbation theory. From the analysis presented in Figs. 1–3 for typical two-body interaction strengths of order $g_{\text{eff}}N/\hbar\omega_x a_x^2 \sim 10^2$ it is already seen that nonlinear rotation strengths of the order $\mathcal{C}Nm/\hbar \sim 10$ are sufficient to observe effects stemming from the nonlinear rotation, which does not violate the assumption $\Delta_d \ll \hbar\Omega_r$.

Figure 2 shows example solutions for different fixed parameters. Figure 2(a) shows example chemical potentials $\mu'/\hbar\omega_x$ calculated as a function of the trap anisotropy for three fixed individual values of the two-body mean-field interaction strength $g_{\text{eff}}N/\hbar\omega_x a_x^2 = 1 \times 10^2, 3 \times 10^2, 5 \times 10^5$. We observe that the point at which the solutions terminate shifts to larger values of $\mu'/\hbar\omega_x$ as the two-body mean-field strength is increased. Figure 2(b) shows the chemical potential as a function of the nonlinear rotation strength, for different fixed values of the trap anisotropy with $g_{\text{eff}}N/\hbar\omega_x a_x^2 = 3 \times 10^2$. Here the nonlinear rotation strength $\mathcal{C}$ attains a maximum value for the case of cylindrical symmetry ($\omega_y = \omega_x$) and is found to possess a maximum value that is always smaller than this for $\omega_y > \omega_x$ and $\omega_y < \omega_x$, i.e., as the cloud goes from a quasi-two to quasi-one-dimensional geometry. Figure 2(c) depicts four example solutions with $\omega_y/\omega_x = 0.75, 1, 1.5, 2$ in the (g_{eff}, $\mathcal{C}$) parameter space with constant $\mu'/\hbar\omega_x = 10$. Again the point of cylindrical symmetry ($\omega_y = \omega_x$) represents the point with the largest range of solutions for $\mathcal{C}$, while either reducing or increasing the anisotropy of the harmonic trap always reduces the range of available solutions, similar to Fig. 2(b). Meanwhile, Fig. 2(d) shows example solutions for fixed $\mu'/\hbar\omega_x = 10$ and $\mathcal{C}Nm/\hbar = 10$ in the (g_{eff}, ω_y/ω_x) parameter space. Plotted on a log-log scale, these solutions are revealed to be quasilinear, with a maximum and minimum allowed solution for a given fixed pair of parameters. Increasing the chemical potential μ' has the effect of shifting the solutions to higher g_{eff}, as well as simultaneously increasing the overall observed range of ω_y/ω_x for a given pair of parameters.

It is also also important to consider the validity of the theory in terms of the local density approximation. On physical grounds this amounts to the size of an individual vortex core being much smaller than the size of the condensate; consequentially, the healing length $\xi = \hbar/\sqrt{m\mu'}$ of the vortex must be much smaller than the Thomas-Fermi length scales $R_{x,y}$ or

$$\frac{\xi}{R_{x,y}} = \begin{cases} \frac{\hbar\omega_x}{\sqrt{2}\mu'} \ll 1 & \text{for } x \\ \frac{\hbar\omega_x}{\sqrt{2}\mu'}\frac{\omega_y}{\omega_x} \ll 1 & \text{for } y. \end{cases} \tag{25}$$

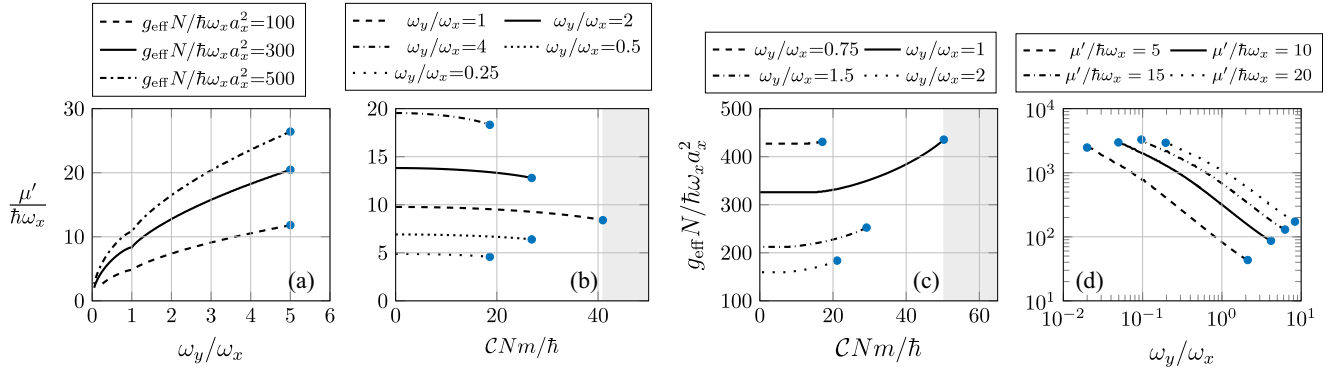FIG. 2. Fixed parameter solutions to Eq. (19): chemical potential μ' for fixed (a) interaction strength g_{eff} and (b) trap anisotropy ω_y/ω_x, (c) allowed solutions for fixed $\mu'/\hbar\omega_x = 10$ and ω_y/ω_x obtained from Eq. (19) in the $(g_{\text{eff}}, \mathcal{C})$ parameter space, and (d) allowed solutions for fixed μ' in the $(g_{\text{eff}}, \omega_y)$ parameter space with $\mathcal{C}Nm/\hbar = 10$. The gray shaded regions in (b) and (c) indicate the boundary to maximum nonlinear rotation for $\omega_y = \omega_x$.

Figure 3 presents numerical calculations of the ratio $\xi/R_{x,y}$. Figures 3(a) and 3(b) show ξ/R_x and ξ/R_y, respectively, for fixed two-body interaction strength $g_{\text{eff}}N/\hbar\omega_x a_x^2 = 300$, for various fixed trap anisotropies $\omega_y/\omega_x = \frac{1}{4}, \frac{1}{2}, 1, 2, 4$. In all cases Eq. (25) is satisfied. Figure 3(c) shows instead $\xi/R_{x,y}$ computed as a function of ω_y/ω_x for various fixed two-body interaction strengths. The data for ξ/R_x (green) are monotonically decreasing on the interval $0 < \omega_y/\omega_x \leqslant 5$, whereas the data for ξ/R_y (blue) monotonically increase on this interval. This can be interpreted in a straightforward way: For $\omega_y/\omega_x < 1$ the data for ξ/R_x show that the local density approximation is not as good as for $\omega_y/\omega_x > 1$. This situation is reversed for the equivalent ξ/R_y data, where the local density approximation is instead improving for $\omega_y/\omega_x < 1$. Finally, the three schematic diagrams above Fig. 3(b) illustrate the three situations $\omega_y/\omega_x < 1$, $\omega_y/\omega_x = 1$, and $\omega_y/\omega_x > 1$. For the case of cylindrical symmetry we can write down an exact

form of Eq. (25) using Eqs. (22) and (23), giving

$$\sqrt{\frac{\pi \ln 2}{N}} \frac{\hbar}{\sqrt{mg_{\text{eff}}}} \ll 1. \tag{26}$$

Finally, let us comment on the presence of the cusps that appear in Figs. 1(a) and 1(c), Fig. 2(a), and also Fig. 3(c) at the symmetry point $\omega_y = \omega_x$. Examining the mathematical structure of Eq. (19), we note that the first two terms on the left-hand side are a difference of inverse hyperbolic sines whose arguments involve square roots of the function $(\omega_y^2/\omega_x^2 - 1)^{-1}$ which is sharply peaked around the symmetry point $\omega_y = \omega_x$. The difference of these two functions (the argument of the second is shifted with respect to first by a factor of $1 - \alpha^2$, which effectively removes the singularity at $\omega_y = \omega_x$) can be understood as the origin of these cusps. As the solutions are continuous through the symmetry point in these examples, these cusps can be understood as an
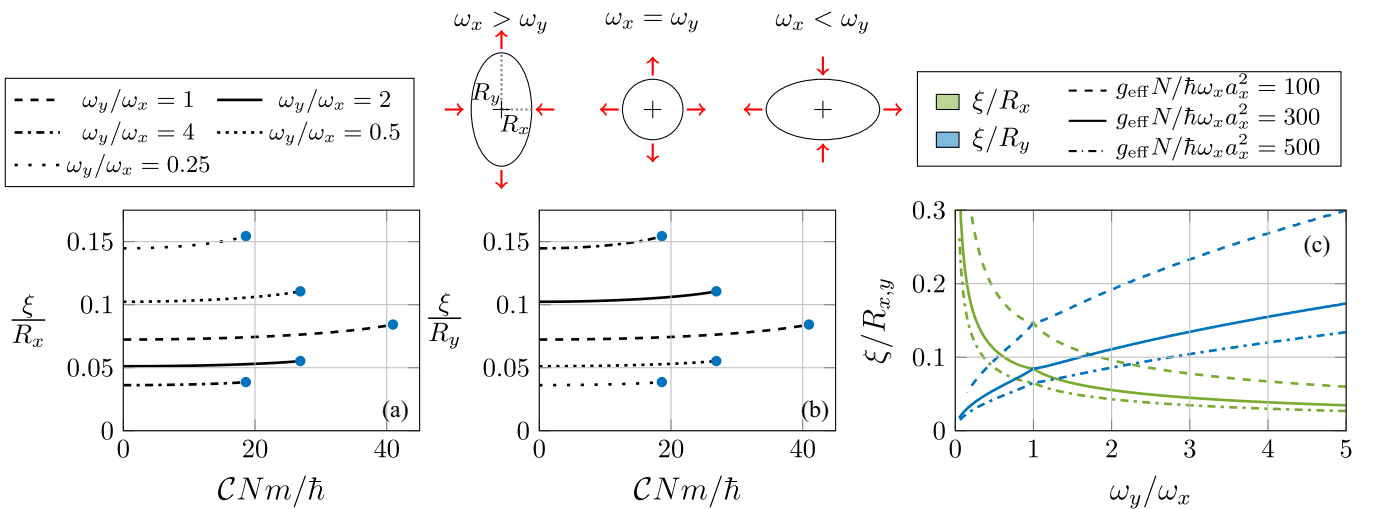

FIG. 3. Local density approximation. (a) and (b) Ratio $\xi/R_{x,y}$ with constant $g_{\text{eff}}N/\hbar\omega_x a_x^2 = 300$ throughout for various fixed ω_y/ω_x as a function of $\mathcal{C}$ and (c) ratio $\xi/R_{x,y}$ as a function of ω_y/ω_x. The three schematic diagrams above (b) show the geometry of the cloud for $\omega_y/\omega_x < 1$, $\omega_y/\omega_x = 1$, and $\omega_y/\omega_x > 1$.
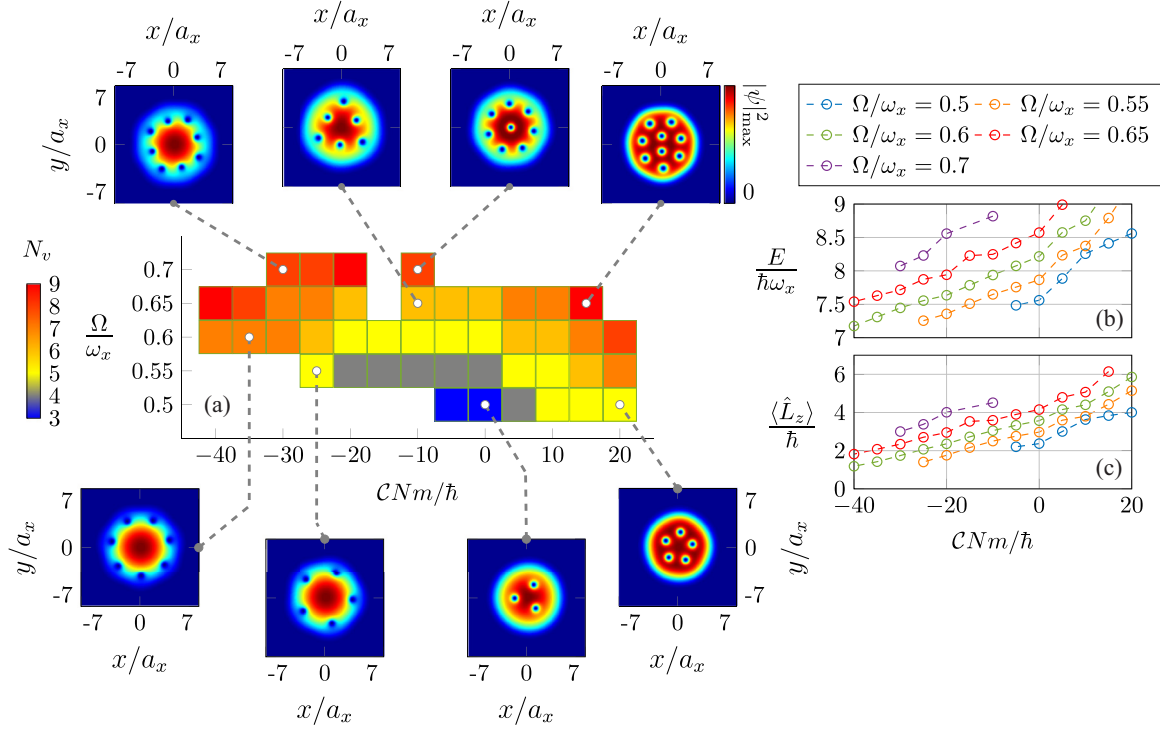
FIG. 4. Vortex ground-state diagram. (a) Number of vortices N_v as a function of the rigid-body Ω and nonlinear rotation strengths $\mathcal{C}$ for 44 individual ground states. Example ground states $|\psi(x, y)|^2$ are shown for different choices of $(\Omega, \mathcal{C})$, indicated by the gray dashed lines. Also shown are (b) the energy E computed using Eq. (28) and (c) the angular momentum $\langle \hat{L}_z \rangle$ corresponding to the data presented in (a).

interesting mathematical artifact of Eq. (19), rather than having any measurable physical consequence in a potential experimental.

D. Existence of stationary solutions

Since this model [Eq. (12)] possesses an unusual nonlinear structure, it is important to consider the nature of the nonlinear solutions and in particular their dynamical behavior. Since the model is Hermitian, the dynamical evolution of solutions obtained from the regions of the parameter space where they exist are stationary with a well-defined energy. An explicit way to see this is to switch to the hydrodynamic picture using the Madelung transformation $\psi(\mathbf{r}, t) = \sqrt{n(\mathbf{r}, t)} \exp[i\vartheta(\mathbf{r}, t)]$, giving

$$\frac{\partial n(\mathbf{r})}{\partial t} + \nabla \cdot \left(n(\mathbf{r}) \left\{ \mathbf{v}_\vartheta - \frac{1}{2} [\mathbf{\Omega}(\boldsymbol{\rho}, t) + \mathbf{\Omega}] \times \boldsymbol{\rho} \right\} \right) = 0,$$

(27)

where $\mathbf{v}_\varphi = \hbar \nabla \vartheta / m$, $\mathbf{\Omega}(\mathbf{r}, t) = \hat{e}_z \Omega(\mathbf{r}, t)$, and $\mathbf{\Omega} = \hat{e}_z \Omega$. Equation (12) has the form of a standard rotating conservation law for the probability density and does not depend on any additional terms that constitute loss or gain of probability density. From this we can conclude that the associated solutions are stationary, which we explore in the next section.

III. NUMERICAL RESULTS

A. Isotropic nonlinear rotation

In this section we explore the numerical stationary-state solutions to the generalized Schrödinger equation (12) for different physical conditions. These solutions are calculated

using a finite-difference scheme, the details of which are provided in the Appendix. Understanding the possible vortex configurations in superfluid systems remains an ongoing interest; see, for example, Refs. [88–90] for recent studies.

In this section we begin by considering the possible ground-state configurations of Eq. (12) in the parameter space of the rigid-body and nonlinear rotation strength $(\Omega, \mathcal{C})$ for fixed trap anisotropy $\omega_y / \omega_x = 1.01$ and two-body mean-field strength $g_{\text{eff}} N / \hbar \omega_x a_x^2 = 3 \times 10^2$. Note that in order to nucleate vortices in this system we require a finite rigid-body rotation strength ($\Omega > 0$) since the vorticity would otherwise be zero at the edges of the system due to the presence of the trapping potential. In Fig. 4 the number of vortices N_v is presented in the $(\Omega, \mathcal{C})$ parameter space, allowing us to interpret the effect of these two parameters on both the morphology and topology of the superfluid state. In general, increasing Ω for fixed nonlinear rotation strength $\mathcal{C}$ increases the observed number of vortices. If instead we fix the rigid-body rotation strength Ω, we find that the number of vortices increases with the modulus of $\mathcal{C}$. The morphology of the superfluid is strongly affected by the choice of $\mathcal{C}$. For large positive $\mathcal{C}$ the vortices tend to localize; for example, the ground-state densities $|\psi(x, y)|^2$ for $(\Omega/\omega_x = 0.5, \mathcal{C}Nm/\hbar = 20)$ and $(\Omega/\omega_x = 0.65, \mathcal{C}Nm/\hbar = 15)$ show tightly packed arrangements (five and nine vortices, respectively). On the other hand, for large negative $\mathcal{C}$ the vortices tend to delocalize into ring structures; for example, $(\Omega/\omega_x = 0.55, \mathcal{C}Nm/\hbar = -25)$ and $(\Omega/\omega_x = 0.6, \mathcal{C}Nm/\hbar = -35)$ each shows a single ring of five and seven vortices, respectively. As well as the ring arrangements, we also observe concentric ring configurations. For $(\Omega/\omega_x = 0.65, \mathcal{C}Nm/\hbar = -10)$ a pair of rings formed

from individual triangular vortex patterns is observed, while for $(\Omega/\omega_x = 0.7, \mathcal{C}Nm/\hbar = -30)$ a pair of rings constructed from vortices occupying the vertices of two squares is found. It is also possible to find a ground state comprising a single ring of vortices surrounding a single vortex at the origin of the harmonic trap, as shown for $(\Omega/\omega_x = 0.7, \mathcal{C}Nm/\hbar = -10)$. Figures 4(b) and 4(c) show the energy of the individual ground states computed from the definition

$$E = \int d\boldsymbol{\rho} \left[\frac{\hbar^2}{2m} |\boldsymbol{\nabla}\psi|^2 + V|\psi|^2 + \frac{g_{\mathrm{eff}}}{2}|\psi|^4 - \boldsymbol{\Omega} \cdot \psi^* \hat{L}_z \psi \right], \tag{28}$$

which for a fixed value of Ω increases monotonically as a function of $\mathcal{C}$. Intuitively, we can understand this behavior since vortices at the edge of the cloud are localized in a low-density region and have a lower energy than those at larger values of $\mathcal{C}$ that may be closer to the center of the trap, possessing a corresponding larger ground-state energy. Figure 4(c) displays the mean value of the angular momentum, computed from $\langle \hat{L}_z \rangle = \int d\boldsymbol{\rho} \, \psi^* \hat{L}_z \psi$. Again the computed value of $\langle \hat{L}_z \rangle$ monotonically increases from negative to positive $\mathcal{C}$ for fixed Ω, due to the effect of the background of the trapped cloud modulating $\langle \hat{L}_z \rangle$ with the position of the vortices. We can also understand the unusual vortex phenomenology present in this system by considering the (averaged) vorticity, defined as $\boldsymbol{\omega}_v = \boldsymbol{\nabla} \times \mathbf{v}$ [91], where $\mathbf{v} = \Omega(\rho, t)\hat{e}_z \times \boldsymbol{\rho}$. Using these two definitions, we can show that

$$\boldsymbol{\omega}_v = \hat{e}_z \left[2\Omega(\rho, t) + \rho \frac{\partial \Omega(\rho, t)}{\partial \rho} \right]. \tag{29}$$

The vorticity given by Eq. (29) varies in both time and space. This can be used to interpret the unusual vortex arrangements described in this work. Here the second (different) term appearing in Eq. (29) depends on the radial derivative of the atomic density [Eq. (18)], leading to a contribution to the vorticity that depends on the local radial curvature of the state.

B. Elliptical trap deformation

Next we explore the effect of varying the strength of the nonlinear rotation strength while fixing both the trap anisotropy and rigid-body rotation strengths. Although angular momentum is no longer conserved when $\omega_y \neq \omega_x$, stationary states of the generalized Gross-Pitaevskii model [Eq. (12)] can still be obtained in the rotating frame in a similar spirit to Refs. [24,27] where stationary states were obtained for nonaxisymmetric confined gases for finite rigid-body rotation. Figure 5 explores the effect of computing the ground states of Eq. (12) in two configurations: the first with constant $\omega_y/\omega_x = 1.25$ and $\Omega/\omega_x = 0.6$ and the second with constant $\omega_y/\omega_x = 1.5$ and $\Omega/\omega_x = 0.8$. Note that the change in the rigid-body strength here is to accommodate the fact that working at larger values of the trap anisotropy ω_y/ω_x tends to reduce the observed number of vortices; hence Ω/ω_x is slightly increased for the case of $\omega_y/\omega_x = 1.5$. Figure 5(a) shows the ground-state energy E (left axis) computed using Eq. (28) and corresponding angular momentum $\langle \hat{L}_z \rangle$ (right axis). The energy of the ground states, shown as blue pluses and crosses, is found to be increasing from negative to positive
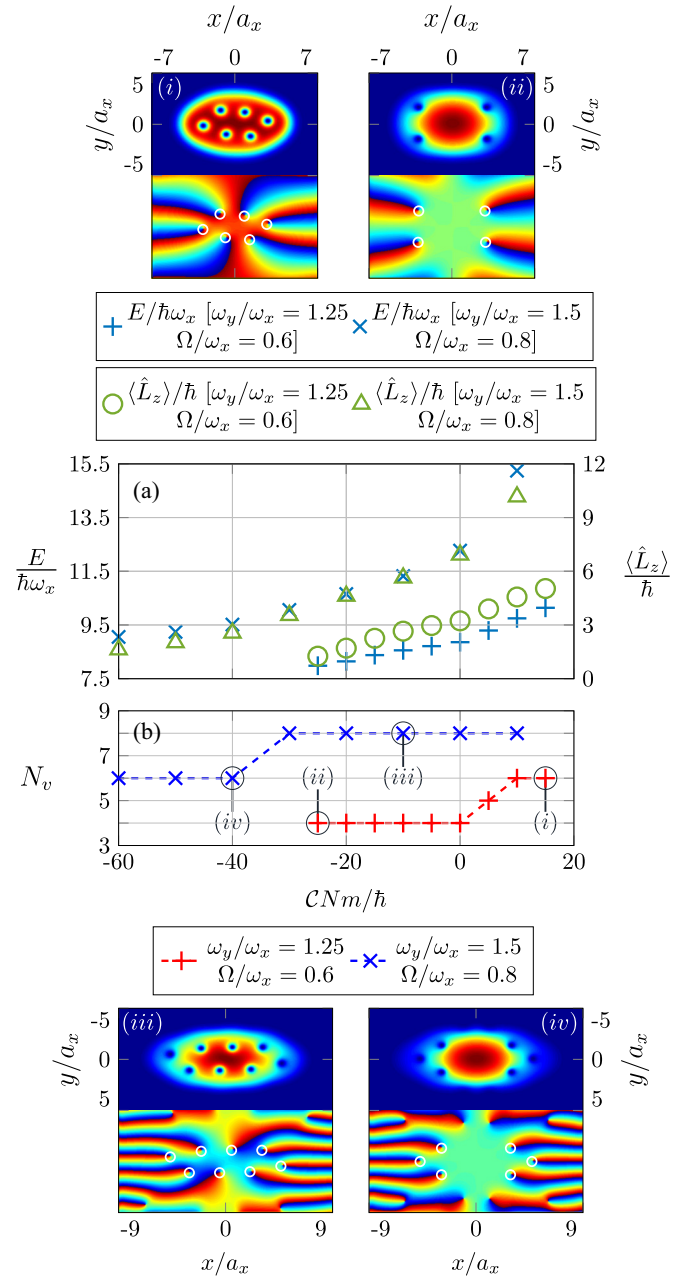

FIG. 5. Nonlinear elliptical rotation ground states. (a) Energy (blue pluses and crosses) calculated using Eq. (28) and angular momentum $\langle \hat{L}_z \rangle$ (green circles and triangles) computed for the trapping anisotropies $\omega_y/\omega_x = 1.25, 1.5$ as a function of the nonlinear rotation strength. (b) Corresponding number of vortices N_v as a function of $\mathcal{C}Nm/\hbar$. Four example ground-state density and phases are also shown, labeled (i)–(iv) in (b).

values of $\mathcal{C}Nm/\hbar$. Again, as described in Sec. III A, this is due to the vortices tending to delocalize at the edges of the harmonic trap for $\mathcal{C} \ll 0$, resulting in a lower overall energy. Meanwhile, for large (positive) $\mathcal{C}$ the vortices are localized closer to the center of the trap, resulting in a (relatively) higher ground-state energy. The angular momentum is shown as green circles and triangles and shows a similar trend to the energy, increasing from negative to positive $\mathcal{C}$. We also note that increasing the trap anisotropy ω_y/ω_x has the effect
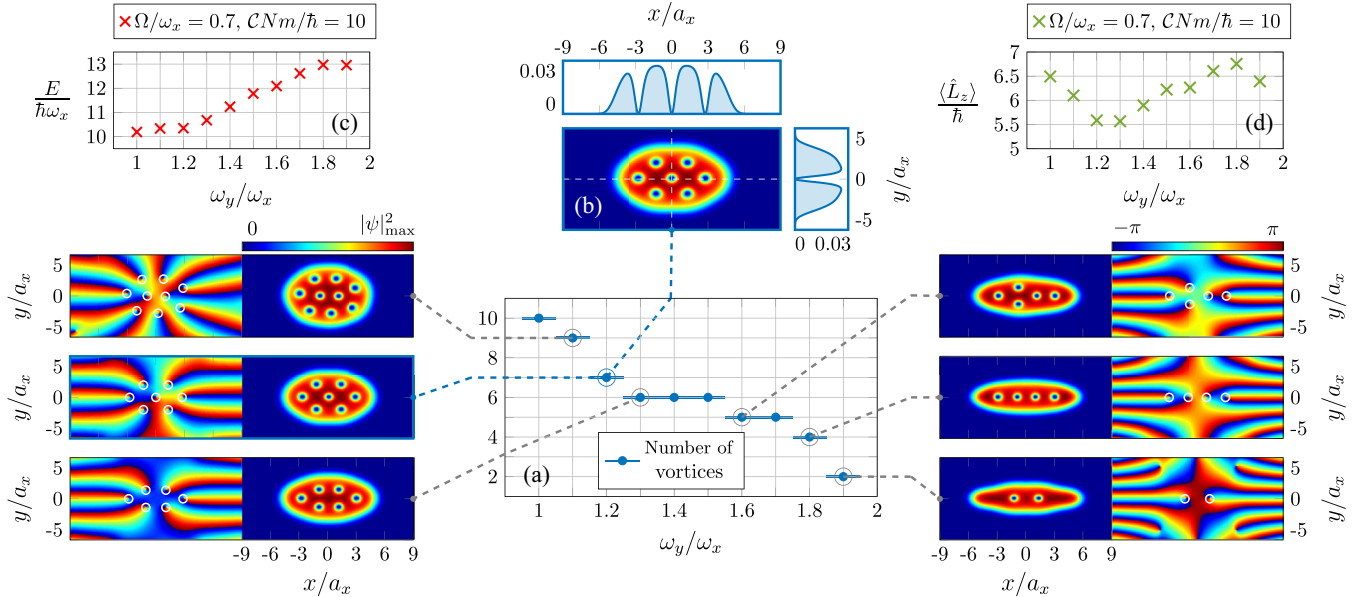
FIG. 6. Deformed trap ground states. (a) Number of vortices computed as a function of the trap anisotropy ω_y/ω_x; the dashed arrows connect example ground states for different anisotropies. Example ground states show the density and phase, with vortices highlighted in the phase. (b) Density for $\omega_y/\omega_x = 1.2$ with accompanying Cartesian cross sections of the density. Also shown are the associated (c) energy and (d) angular momentum. Throughout $\Omega/\omega_x = 0.7$ and $\mathcal{C}Nm/\hbar = 10$.

of reducing the amount by which the energy and angular momentum vary. Figure 5(b) shows the number of vortices N_v for both configurations presented in Fig. 5(a). Interestingly, we find that there exists a value of the nonlinear rotation strength $\mathcal{C}$ where the number of vortices is reduced but does not increase again, in contrast to the situation with cylindrical trap symmetry described previously in Sec. III A. We attribute this behavior to the breaking of conservation of angular momentum, since the density-dependent rotation in the trapped limit essentially depends on the shape of the harmonic confinement which becomes elliptical for $\omega_y \neq \omega_x$. Finally, in Fig. 5 there are several example ground states, labeled (i)–(iv), showing different vortical configurations for parameters shown in Fig. 5(b), with the top panels in each example showing the density $|\psi(x, y)|^2$ while the bottom panels show the associated phase distribution $\vartheta(\boldsymbol{\rho}) = \tan^{-1}\{\text{Im}(\psi)/\text{Re}(\psi)\}$. The individual vortices are highlighted in the phase with white circles.

We can also investigate the effect on the superfluid state by fixing both of the rotational parameters Ω and $\mathcal{C}$ and instead varying the ellipticity of the harmonic confinement through ω_y/ω_x. Numerical simulations of this situation are presented in Fig. 6 for $\Omega/\omega_x = 0.7$ and $\mathcal{C}Nm/\hbar = 10$. Figure 6(a) displays the number of vortices N_v as a function of the trap anisotropy. As the trap geometry is gradually reduced from the quasi-two-dimensional ($\omega_y \sim \omega_x$) to quasi-one-dimensional ($\omega_y \gtrsim \omega_x$) limit, the number of observed vortices decreases, consistent with the known behavior of anisotropically confined phase defects [26]. Six individual ground-state configurations are also presented for different values of the trap anisotropy ω_y/ω_x. We observe that close to the cylindrical $\omega_y \sim \omega_x$ limit the vortices adopt almost triangular configurations, while for $\omega_y/\omega_x = 1.8, 1.9$ the vortices instead adopt a one-dimensional alignment as well as being

reduced in number. Figure 6(b) displays the ground-state density $|\psi(x, y)|^2$ for $\omega_y/\omega_x = 1.2$, as well as accompanying Cartesian cross sections $|\psi(x, y = 0)|^2$ (top panel) and $|\psi(x = 0, y)|^2$ (right panel) showing the cores of the vortices for this example. Figures 6(c) and 6(d) show the corresponding ground-state energy E [Eq. (28)] and angular momentum $\langle \hat{L}_z \rangle$, respectively. The ground-state energy E is observed to increase monotonically with ω_y/ω_x, again consistent with the known behavior of these systems [viz., Eq. (17)]. Finally, Fig. 6(d) showing the angular momentum $\langle \hat{L}_z \rangle$ is observed to oscillate as the trap anisotropy is increased, an unusual and unexpected result, since increasing ω_y/ω_x typically causes a reduction of the angular momentum, since the number of vortices is reduced at larger trapping anisotropies. This is likely due to the nontrivial effect of nonlinear rotation, which directly couples the deformed atomic density and the angular momentum of the condensate.

C. Vortex lattices and rings

In this section we examine the effect of the interplay of rigid-body and nonlinear rotation when there is significant vorticity, for the almost cylindrical trap $\omega_y/\omega_x = 1.01$. For the case of pure rigid-body rotation ($\mathcal{C} = 0$) it is well established that for large rotational driving strengths $\Omega \sim \omega_x$ dense triangular arrangements of vortices are observed. The presence of the nonlinear rotation in Eq. (12) is expected to give rise to unusual many-vortex states, since we know that the presence of this term modifies the morphology of the vortex arrangements. Recent related work has also revealed the vortex patterns of bosonic systems with long-range statistical interactions [92], a cousin of the model considered in this work.

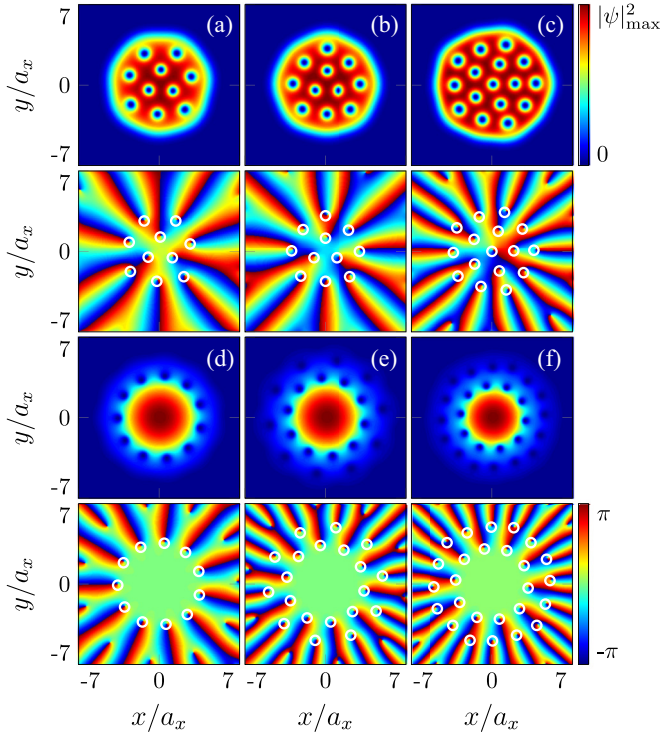Figure 7 shows several example stationary states possessing significant vorticity. In Figs. 7(a)–7(c) the atomic

FIG. 7. Vortex lattices and rings. (a)–(c) Atomic density $|\psi|^2$ for fixed $\mathcal{C}Nm/\hbar = 10$ and (a) $\Omega/\omega_x = 0.7$, (b) $\Omega/\omega_x = 0.75$, and (c) $\Omega/\omega_x = 0.85$, with the corresponding phase shown in each panel below. (d)–(f) Atomic density $|\psi|^2$ for fixed nonlinear rotation strength $\mathcal{C}Nm/\hbar = -60$ and (d) $\Omega/\omega_x = 0.75$, (e) $\Omega/\omega_x = 0.8$, and (f) $\Omega/\omega_x = 0.85$, again with the phase distributions shown below in each case. Throughout $\omega_y/\omega_x = 1.01$.

density is presented corresponding to the fixed nonlinear rotation strength $\mathcal{C}Nm/\hbar = 10$ for increasing rigid-body driving strengths $\Omega/\omega_x = 0.7, 0.75, 0.85$, respectively. We can observe that the increasing number of vortices $N_v = 10, 11, 16$ in these examples arrange into a triangular pattern; however, it would seem that as Ω/ω_x increases the density of the vortices also grows. We would speculate that this is an effect of the boundaries of the cloud, which as we move to higher rotational driving strengths become more deformed due to the nonlinear rotation and hence contribute more in this limit to the deformation of the observed vortex lattice. In each case, the corresponding phase distribution is shown in the panels directly below Figs. 7(a)–7(c), with the vortices highlighted by white circles. Figures 7(d)–7(f) show stationary states obtained for fixed $\mathcal{C}Nm/\hbar = -60$, again with increasing rigid-body rotation $\Omega/\omega_x = 0.75, 0.8, 0.85$, with the respective number of vortices being $N_v = 11, 20, 26$. Again, for $\mathcal{C} < 0$ we observe the spatial delocalization of the vortices and the absence of the triangular Abrikosov vortex lattice. Instead, the vortices tend to arrange into ring structures, as observed in Fig. 7(d). Interestingly, as Ω/ω_x is increased, concentric (double) ring structures can also be obtained, as shown in Figs. 7(e) and 7(f). We can see that the shape of the background condensate is quite different for the examples presented in Figs. 7(a)–7(c) with $\mathcal{C} > 0$ and Figs. 7(d)–7(f) with $\mathcal{C} < 0$, due to the underlying generalized

(rotating) density distribution $n(\rho)$ [Eq. (18)] possessing a distorted form compared to the standard Thomas-Fermi distribution. As before, the corresponding phase distributions are presented below Figs. 7(d)–7(f) and the vortices are highlighted with white circles.

IV. SUMMARY

In this work we have examined theoretically the few- to many-vortex states of a gas of bosons confined in an elliptical harmonic trap, subject to a density-dependent gauge potential that manifests as an effective density-angular-momentum coupling to the atomic condensate. By constructing analytical and semianalytical solutions in the Thomas-Fermi limit, the stability of the nonlinear system was probed as a function of the anisotropy of the confinement and strengths of the nonlinear rotation and two-body interactions. This in turn revealed stable and unstable regions of the parameter space, the condensate being stable over the largest parameter values (nonlinear rotation strength) close to the cylindrical limit, while for more quasi-one-dimensional configurations the stable regions of the total parameter space were found to be more restricted.

Numerical simulations of the generalized Schrödinger equation revealed the vortical phenomenology, including the topology and morphology of the various ground states of the rotating system. Close to cylindrical confinement, different vortex patterns were presented, exploring the interplay of the nonlinear rotation and the rigid-body rotation. Vortex ring arrangements were observed and attributed to the effect of the unusual vorticity present in the system. Following this, the effect of elliptical harmonic trapping was studied. Here the trap aspect ratio was fixed while the strength of the nonlinear rotation was varied, revealing a critical point where the vortices separate into opposing regions of the trapped cloud, an effect caused by the spatially varying vorticity. Then the effect of fixing the nonlinear rotation strength and changing the trap ellipticity was investigated. It was found that, similar to the case of rigid-body rotation, increasing the trap anisotropy from a quasi-two- to quasi-one-dimensional limit causes the total number of observed vortices to decrease. Finally, we considered the effect of the density-angular-momentum coupling at larger rigid-body rotation strengths in an almost cylindrical trap. It was found that for large positive nonlinear rotation strengths vortex lattices with increasingly densely arranged vortices are observed, while instead for large negative nonlinear rotation strength the vortices arrange into single ring and (multiple) concentric ring structures.

This work has explored the effect of elliptical density-angular-momentum coupling in quasi-two-dimensional atomic Bose-Einstein condensates, revealing the exotic phenomenology of this unusual physical system. As well as being interesting from a fundamental physics perspective, exotic superfluid systems such as those considered in this work also provide an important potential resource for quantum technologies. One potential application in this realm is the emerging field of atomtronics, which aims to harness cold-atom systems to realize, e.g., analogies of classical electronic circuits [93]. In this sense the density-dependent gauge theory studied in this work possesses a spatially

varying vorticity which could be exploited to realize atomtronic circuits with radial symmetry without the need for complicated ring trap potentials [94], due to the ability to realize ring vortex arrangements in a standard harmonic trap with the system studied in this work. In the future it would be interesting, for example, to understand experimentally motivated dynamical effects associated with dimensional crossovers, such as vortex solitons and solitonic vortices, as well as beyond mean-field effects such as density-dependent quantum droplets.

ACKNOWLEDGMENTS

APPENDIX: NUMERICAL SIMULATIONS

In this Appendix we outline the methodology used to compute the numerical solutions presented in Sec. III. Essentially, we propagate the generalized Schrödinger equation (12) in imaginary time using the discretization

$$
i\hbar \left[\frac{\psi_{j,k}^{n+1} - \psi_{j,k}^n}{\Delta t} \right]
$$

$$
= -\frac{\hbar^2}{2m} \left[\frac{\psi_{j+1,k}^n - 2\psi_{j,k}^n + \psi_{j-1,k}^n}{\Delta x^2} \right.
$$

$$
\left. + \frac{\psi_{j,k+1}^n - 2\psi_{j,k}^n + \psi_{j,k-1}^n}{\Delta y^2} \right]
$$

$$
+ V_{j,k}\psi_{j,k}^n + i\hbar\big(\Omega + \mathcal{C}\big|\psi_{j,k}^n\big|^2\big)
$$

$$
\times \left[x_j \left\{ \frac{\psi_{j,k+1}^n - \psi_{j,k-1}^n}{2\Delta y} \right\} - y_k \left\{ \frac{\psi_{j+1,k}^n - \psi_{j-1,k}^n}{2\Delta x} \right\} \right]
$$

$$
+ g_{\text{eff}}\big|\psi_{j,k}^n\big|^2 \psi_{j,k}^n, \tag{A1}
$$

where the continuous wave function $\psi(x, y, t)$ becomes the discrete variable $\psi_{j,k}^n$. The spatial and temporal grid sizes are defined as Δx, Δy and Δt, respectively, and numerical stability requires $\Delta t / \Delta\{x, y\}^2 < \frac{1}{2}(\omega_x a_x^2)^{-1}$. In our simulations we used $\Delta x = \Delta y = 0.05 a_x$ and $\Delta t = 5 \times 10^{-5}(\omega_x)^{-1}$.

Figure 8 shows data recorded from two example imaginary-time runs for different physical parameters. Figure 8(a) shows $E[t_n] - E[t_N]$, i.e., the difference between the energy recorded after the nth sample and the final sample N, where each sample is recorded after every 2×10^5 iterations. Figure 8(b) shows instead the difference between consecutive samples $E[t_{n-1}] - E[t_n]$ plotted semilogarithmically. The initial condition $\psi_{j,k}^0$ for each run is taken as a pseudorandom matrix, which breaks any underlying symmetries and stops
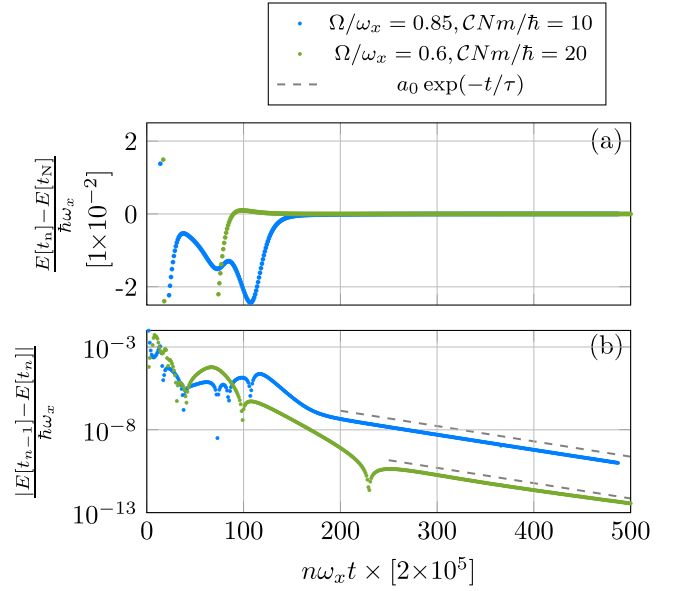

FIG. 8. Imaginary-time ground-state calculations: (a) example data for the difference of the sampled energy during imaginary time and the final energy and (b) difference between the consecutively sampled energies. The two gray lines are a fit [see Eq. (A2)] during the final equilibration of the vortex pattern.

the simulation from getting stuck in any metastable states. Note that for a finite (trapped) system vortices can only be nucleated if $\Omega \neq 0$, since phase defects enter the cloud via the boundaries, so one must always work at finite Ω in order to generate vorticity with a density-angular-momentum coupling. Then propagation in imaginary time leads to different dynamical regimes. For $n\omega_x t \lesssim 100$, vortices enter the cloud from the edges of the system and begin to arrange themselves inside the trap. After this for $100 \lesssim n\omega_x t \lesssim 200$ the vortices continue to arrange themselves closer to the equilibrium configuration, which occurs for long times and is heralded by the exponential decay of the energy difference (gray dashed lines) which follows the exponential fit

$$
\frac{|E[t_{n-1}] - E[t_n]|}{\hbar\omega_x} = a_0 \exp(-t/\tau), \quad n \gg 1, \tag{A2}
$$

where $\tau = 47/\omega_x$ and a_0 is a fitting parameter, which gives the converged ground-state configuration. Individual simulations can be terminated after a certain tolerance of the energy difference is obtained. This is typically less than approximately 10^{-10}, although configurations with more vortices present or where there are vortices closer to the edges of the harmonic trap require a smaller tolerance to produce the final high-fidelity ground state.

[1] M. R. Matthews, B. P. Anderson, P. C. Haljan, D. S. Hall, C. E. Wieman, and E. A. Cornell, Vortices in a Bose-Einstein Condensate, Phys. Rev. Lett. **83**, 2498 (1999).

[2] F. Chevy, K. W. Madison, and J. Dalibard, Measurement of the Angular Momentum of a Rotating Bose-Einstein Condensate, Phys. Rev. Lett. **85**, 2223 (2000).

[3] C. Raman, J. R. Abo-Shaeer, J. M. Vogels, K. Xu, and W. Ketterle, Vortex Nucleation in a Stirred Bose-Einstein Condensate, Phys. Rev. Lett. **87**, 210402 (2001).

[4] J. R. Abo-Shaeer, C. Raman, J. M. Vogels, and W. Ketterle, Observation of vortex lattices in Bose-Einstein condensates, Science **292**, 476 (2001).

[5] W. J. Kwon, G. Moon, J.-y. Choi, S. W. Seo, and Y.-i. Shin, Relaxation of superfluid turbulence in highly oblate Bose-Einstein condensates Phys. Rev. A **90**, 063627 (2014).

[6] Z. Hadzibabic, P. Krüger, M. Cheneau, B. Battelier, and J. Dalibard, Berezinskii-Kosterlitz-Thouless crossover in a trapped atomic gas, Nature (London) **441**, 1118 (2006).

[7] L. E. Sadler, J. M. Higbie, S. R. Leslie, M. Vengalattore, and D. M. Stamper-Kurn, Spontaneous symmetry breaking in a quenched ferromagnetic spinor Bose-Einstein condensate, Nature (London) **443**, 312 (2006).

[8] I.-K. Liu, S. Donadello, G. Lamporesi, G. Ferrari, S.-C. Gou, F. Dalfovo, and N. P. Proukakis, Dynamical equilibration across a quenched phase transition in a trapped quantum gas, Commun. Phys. **1**, 24 (2018).

[9] G. Gauthier, M. T. Reeves, X. Yu, A. S. Bradley, M. A. Baker, T. A. Bell, H. Rubinsztein-Dunlop, M. J. Davis, and T. W. Neely, Giant vortex clusters in a two-dimensional quantum fluid, Science **364**, 1264 (2019).

[10] M. Lewenstein, A. Sanpera, and V. Ahufinger, *Ultracold Atoms in Optical Lattices: Simulating Quantum Many-Body Systems* (Oxford University Press, Oxford, 2012).

[11] M. Tomza, K. Jachymski, R. Gerritsma, A. Negretti, T. Calarco, Z. Idziaszek, and P. S. Julienne, Cold hybrid ion-atom systems, Rev. Mod. Phys. **91**, 035001 (2019).

[12] L. Pezzè, A. Smerzi, M. K. Oberthaler, R. Schmied, and P. Treutlein, Quantum metrology with nonclassical states of atomic ensembles, Rev. Mod. Phys. **90**, 035005 (2018).

[13] A. Eckardt, Colloquium: Atomic quantum gases in periodically driven optical lattices, Rev. Mod. Phys. **89**, 011004 (2017).

[14] T. Ozawa, H. M. Price, A. Amo, N. Goldman, M. Hafezi, L. Lu, M. C. Rechtsman, D. Schuster, J. Simon, O. Zilberberg, and I. Carusotto, Topological photonics, Rev. Mod. Phys. **91**, 015006 (2019).

[15] N. R. Cooper, J. Dalibard, and I. B. Spielman, Topological bands for ultracold atoms, Rev. Mod. Phys. **91**, 015005 (2019).

[16] T. W. Neely, E. C. Samson, A. S. Bradley, M. J. Davis, and B. P. Anderson, Observation of Vortex Dipoles in an Oblate Bose-Einstein Condensate, Phys. Rev. Lett. **104**, 160401 (2010).

[17] B. P. Anderson, P. C. Haljan, C. E. Wieman, and E. A. Cornell, Vortex Precession in Bose-Einstein Condensates: Observations with Filled and Empty Cores, Phys. Rev. Lett. **85**, 2857 (2000).

[18] D. R. Scherer, C. N. Weiler, T. W. Neely, and B. P. Anderson, Vortex Formation by Merging of Multiple Trapped Bose-Einstein Condensates, Phys. Rev. Lett. **98**, 110402 (2007).

[19] A. E. Leanhardt, A. Görlitz, A. P. Chikkatur, D. Kielpinski, Y. Shin, D. E. Pritchard, and W. Ketterle, Imprinting Vortices in a Bose-Einstein Condensate using Topological Phases, Phys. Rev. Lett. **89**, 190403 (2002).

[20] Y. Shin, M. Saba, M. Vengalattore, T. A. Pasquini, C. Sanner, A. E. Leanhardt, M. Prentiss, D. E. Pritchard, and W. Ketterle, Dynamical Instability of a Doubly Quantized Vortex in a Bose-Einstein Condensate, Phys. Rev. Lett. **93**, 160406 (2004).

[21] Y. Castin and R. Dum, Bose-Einstein condensates with vortices in rotating traps, Eur. Phys. J. D **7**, 399 (1999).

[22] J. J. García-Ripoll, G. Molina-Terriza, V. M. Pérez-García, and L. Torner, Structural Instability of Vortices in Bose-Einstein Condensates, Phys. Rev. Lett. **87**, 140403 (2001).

[23] B. Damski and K. Sacha, Changes of the topological charge of vortices, J. Phys. A: Math. Gen. **36**, 2339 (2003).

[24] M. Ö. Oktel, Vortex lattice of a Bose-Einstein condensate in a rotating anisotropic trap, Phys. Rev. A **69**, 023618 (2004).

[25] G. Watanabe and C. J. Pethick, Reversal of the circulation of a vortex by quantum tunneling in trapped Bose systems, Phys. Rev. A **76**, 021605(R) (2007).

[26] S. McEndoo and T. Busch, Small numbers of vortices in anisotropic traps, Phys. Rev. A **79**, 053616 (2009).

[27] S. McEndoo and Th. Busch, Vortex dynamics in anisotropic traps, Phys. Rev. A **82**, 013628 (2010).

[28] K. Kasamatsu, M. Tsubota, and M. Ueda, Vortex Molecules in Coherently Coupled Two-Component Bose-Einstein Condensates, Phys. Rev. Lett. **93**, 250406 (2004).

[29] K. Kasamatsu, M. Tsubota, and M. Ueda, Spin textures in rotating two-component Bose-Einstein condensates, Phys. Rev. A **71**, 043611 (2005).

[30] L. Calderaro, A. L. Fetter, P. Massignan, and P. Wittek, Vortex dynamics in coherently coupled Bose-Einstein condensates, Phys. Rev. A **95**, 023605 (2017).

[31] M. Kobayashi, M. Eto, and M. Nitta, Berezinskii-Kosterlitz-Thouless Transition of Two-Component Bose Mixtures with Intercomponent Josephson Coupling, Phys. Rev. Lett. **123**, 075303 (2019).

[32] R. Navarro, R. Carretero-González, P. J. Torres, P. G. Kevrekidis, D. J. Frantzeskakis, M. W. Ray, E. Altuntaş, and D. S. Hall, Dynamics of a Few Corotating Vortices in Bose-Einstein Condensates, Phys. Rev. Lett. **110**, 225301 (2013).

[33] K. E. Wilson, Z. L. Newman, J. D. Lowney, and B. P. Anderson, *In situ* imaging of vortices in Bose-Einstein condensates, Phys. Rev. A **91**, 023621 (2015).

[34] A. Rakonjac, A. L. Marchant, T. P. Billam, J. L. Helm, M. M. H. Yu, S. A. Gardiner, and S. L. Cornish, Measuring the disorder of vortex lattices in a Bose-Einstein condensate, Phys. Rev. A **93**, 013607 (2016).

[35] J. Dalibard, F. Gerbier, G. Juzeliūnas, and P. Öhberg, Colloquium: Artificial gauge potentials for neutral atoms, Rev. Mod. Phys. **83**, 1523 (2011).

[36] N. Goldman, G. Juzeliūnas, P. Öhberg, and I. B. Spielman, Light-induced gauge fields for ultracold atoms, Rep. Prog. Phys. **77**, 126401 (2014).

[37] Y.-J. Lin, R. L. Compton, A. R. Perry, W. D. Phillips, J. V. Porto, and I. B. Spielman, Bose-Einstein Condensate in a Uniform Light-Induced Vector Potential, Phys. Rev. Lett. **102**, 130401 (2009).

[38] Y.-J. Lin, R. L. Compton, K. Jiménez-García, J. V. Porto, and I. B. Spielman, Synthetic magnetic fields for ultracold neutral atoms, Nature (London) **462**, 628 (2009).

[39] Y-J. Lin, R. L. Compton, K. Jiménez-García, W. D. Phillips, J. V. Porto, and I. B. Spielman, A synthetic electric force acting on neutral atoms, Nat. Phys. **7**, 531 (2011).

[40] Y.-J. Lin, K. Jiménez-García, and I. B. Spielman, Spin-orbit-coupled Bose-Einstein condensates, Nature (London) **471**, 83 (2011).

[41] H.-R. Chen, K.-Y. Lin, P.-K. Chen, N.-C. Chiu, J.-B. Wang, C.-A. Chen, P. Huang, S.-K. Yip, Y. Kawaguchi, and Y.-J.

Lin, Spin-Orbital-Angular-Momentum Coupled Bose-Einstein Condensates, Phys. Rev. Lett. **121**, 113204 (2018).

[42] P.-K. Chen, L.-R. Liu, M.-J. Tsai, N.-C. Chiu, Y. Kawaguchi, S.-K. Yip, M.-S. Chang, and Y.-J. Lin, Rotating Atomic Quantum Gases with Light-Induced Azimuthal Gauge Potentials and the Observation of the Hess-Fairbank Effect, Phys. Rev. Lett. **121**, 250401 (2018).

[43] D. Zhang, T. Gao, P. Zou, L. Kong, R. Li, X. Shen, X.-L. Chen, S.-G. Peng, M. Zhan, H. Pu, and K. Jiang, Ground-State Phase Diagram of a Spin-Orbital-Angular-Momentum Coupled Bose-Einstein Condensate, Phys. Rev. Lett. **122**, 110402 (2019).

[44] P. Wang, Z.-Q. Yu, Z. Fu, J. Miao, L. Huang, S. Chai, H. Zhai, and J. Zhang, Spin-Orbit Coupled Degenerate Fermi Gases, Phys. Rev. Lett. **109**, 095301 (2012).

[45] L. W. Cheuk, A. T. Sommer, Z. Hadzibabic, T. Yefsah, W. S. Bakr, and M. W. Zwierlein, Spin-Injection Spectroscopy of a Spin-Orbit Coupled Fermi Gas, Phys. Rev. Lett. **109**, 095302 (2012).

[46] I. B. Spielman, Raman processes and effective gauge potentials, Phys. Rev. A **79**, 063613 (2009).

[47] I. Aitchison and A. Hey, *Gauge Theories in Particle Physics: A Practical Introduction* (CRC, Boca Raton, 2013).

[48] D. R. Murray, P. Öhberg, D. Gomila, and S. M. Barnett, Vortex nucleation in Bose-Einstein condensates due to effective magnetic fields, Phys. Rev. A **79**, 063618 (2009).

[49] S.-W. Su, S.-C. Gou, I.-K. Liu, I. B. Spielman, L. Santos, A. Acus, A. Mekys, J. Ruseckas, and G. Juzeliūnas, Position-dependent spin-orbit coupling for ultracold atoms, New J. Phys. **17**, 033045 (2015).

[50] R. Sachdeva and T. Busch, Creating superfluid vortex rings in artificial magnetic fields, Phys. Rev. A **95**, 033615 (2017).

[51] S. S. S. Hejazi, J. Polo, R. Sachdeva, and T. Busch, Symmetry breaking in binary Bose-Einstein condensates in the presence of an inhomogeneous artificial gauge field, Phys. Rev. A **102**, 053309 (2020).

[52] J. Schloss, P. Barnett, R. Sachdeva, and T. Busch, Controlled creation of three-dimensional vortex structures in Bose-Einstein condensates using artificial magnetic fields, Phys. Rev. A **102**, 043325 (2020).

[53] D. Banerjee, M. Dalmonte, M. Müller, E. Rico, P. Stebler, U.-J. Wiese, and P. Zoller, Atomic Quantum Simulation of Dynamical Gauge Fields Coupled to Fermionic Matter: From String Breaking to Evolution after a Quench, Phys. Rev. Lett. **109**, 175302 (2012).

[54] E. Zohar, J. I. Cirac, and B. Reznik, Cold-Atom Quantum Simulator for SU(2) Yang-Mills Lattice Gauge Theory, Phys. Rev. Lett. **110**, 125304 (2013).

[55] L. Tagliacozzo, A. Celi, P. Orland, M. W. Mitchell, and M. Lewenstein, Simulation of non-Abelian gauge theories with optical lattices, Nat. Commun. **4**, 2615 (2013).

[56] M. J. Edmonds, M. Valiente, G. Juzeliūnas, L. Santos, and P. Öhberg, Simulating an Interacting Gauge Theory with Ultracold Bose Gases, Phys. Rev. Lett. **110**, 085301 (2013).

[57] T. Keilmann, S. Lanzmich, I. McCulloch, and M. Roncaglia, Statistically induced phase transitions and anyons in 1D optical lattices, Nat. Commun. **2**, 361 (2011).

[58] S. Greschner, G. Sun, D. Poletti, and L. Santos, Density-Dependent Synthetic Gauge Fields Using Periodically Modulated Interactions, Phys. Rev. Lett. **113**, 215303 (2014).

[59] S. Greschner, D. Huerga, G. Sun, D. Poletti, and L. Santos, Density-dependent synthetic magnetism for ultracold atoms in optical lattices, Phys. Rev. B **92**, 115120 (2015).

[60] M. Jamotte, N. Goldman, and M. Di Liberto, Strain and pseudo-magnetic fields in optical lattices from density-assisted tunneling, arXiv:2104.13394.

[61] M. J. Edmonds, M. Valiente, and P. Öhberg, Elementary excitations of chiral Bose-Einstein condensates, Europhys. Lett. **110**, 36004 (2015).

[62] J.-h. Zheng, B. Xiong, G. Juzeliūnas, and D.-W. Wang, Topological condensate in an interaction-induced gauge potential, Phys. Rev. A **92**, 013604 (2015).

[63] R. J. Dingwall, M. J. Edmonds, J. L. Helm, B. A. Malomed, and P. Öhberg, Non-integrable dynamics of matter-wave solitons in a density-dependent gauge theory, New J. Phys. **20**, 043004 (2018).

[64] U. Aglietti, L. Griguolo, R. Jackiw, S.-Y. Pi, and D. Seminara, Anyons and Chiral Solitons on a Line, Phys. Rev. Lett. **77**, 4406 (1996).

[65] R. J. Dingwall and P. Öhberg, Stability of matter-wave solitons in a density-dependent gauge theory, Phys. Rev. A **99**, 023609 (2019).

[66] P. Öhberg and E. M. Wright, Quantum Time Crystals and Interacting Gauge Theories in Atomic Bose-Einstein Condensates, Phys. Rev. Lett. **123**, 250402 (2019).

[67] I. A. Bhat, S. Sivaprakasam, and B. A. Malomed, Modulational instability and soliton generation in chiral Bose-Einstein condensates with zero-energy nonlinearity, Phys. Rev. E **103**, 032206 (2021).

[68] M. J. Edmonds, M. Valiente, and P. Öhberg, On the Josephson effect in a Bose-Einstein condensate subject to a density-dependent gauge potential, J. Phys. B **46**, 134013 (2013).

[69] M. F. Saleh and P. Öhberg, Trapped Bose-Einstein condensates in the presence of a current nonlinearity, J. Phys. B **51**, 045303 (2018).

[70] S. Butera, M. Valiente, and P. Öhberg, Quantized vortices in interacting gauge theories, J. Phys. B **49**, 015304 (2016).

[71] S. Butera, M. Valiente, and P. Öhberg, Vortex dynamics in superfluids governed by an interacting gauge theory, New J. Phys. **18**, 085001 (2016).

[72] M. Edmonds and M. Nitta, Vortex patterns of atomic Bose-Einstein condensates in a density-dependent gauge potential, Phys. Rev. A **102**, 011303(R) (2020).

[73] S. Butera, N. Westerberg, D. Faccio, and P. Öhberg, Curved spacetime from interacting gauge theories, Class. Quantum Grav. **36**, 034002 (2019).

[74] Y. Buggy, L. G. Phillips, and P. Öhberg, On the hydrodynamics of nonlinear gauge-coupled quantum fluids, Eur. Phys. J. D **74**, 92 (2020).

[75] Y. Buggy and P. Öhberg, Gauge transformations and Galilean covariance in nonlinear gauge-coupled quantum fluids, Phys. Rev. A **102**, 033342 (2020).

[76] G. Valentí-Rojas, N. Westerberg, and P. Öhberg, Synthetic flux attachment, Phys. Rev. Research **2**, 033453 (2020).

[77] P. Xu, T.-Shu Deng, W. Zheng, and H. Zhai, Density-dependent spin-orbit coupling in degenerate quantum gases, Phys. Rev. A **103**, L061302 (2021).

[78] L. W. Clark, B. M. Anderson, L. Feng, A. Gaj, K. Levin, and C. Chin, Observation of Density-Dependent Gauge Fields in a Bose-Einstein Condensate Based on Micromotion Control in a

Shaken Two-Dimensional Lattice, Phys. Rev. Lett. **121**, 030402 (2018).

[79] F. Görg, K. Sandholzer, J. Minguzzi, R. Desbuquois, M. Messer, and T. Esslinger, Realization of density-dependent Peierls phases to engineer quantized gauge fields coupled to ultracold matter, Nat. Phys. **15**, 1161 (2019).

[80] V. Lienhard, P. Scholl, S. Weber, D. Barredo, S. de Léséleuc, R. Bai, N. Lang, M. Fleischhauer, H. P. Büchler, T. Lahaye, and A. Browaeys, Realization of a Density-Dependent Peierls Phase in a Synthetic, Spin-Orbit Coupled Rydberg System, Phys. Rev. X **10**, 021031 (2020).

[81] K.-X. Yao, Z. Zhang, and C. Chin, Dynamics of domain walls in a Bose-Einstein condensate driven by density-dependent gauge field, arXiv:2105.15052.

[82] M. Cheneau, S. P. Rath, T. Yefsah, K. J. Günter, G. Juzeliūnas, and J. Dalibard, Geometric potentials in quantum optics: A semi-classical interpretation, Europhys. Lett. **83**, 60001 (2008).

[83] J. Ye, H. J. Kimble, and H. Katori, Quantum State Engineering and Precision Metrology Using State-Insensitive Light Traps, Science **320**, 1734 (2008).

[84] S. Butera, Synthetic gauge potentials and analogue gravity in Bose-Einstein condensates, Ph.D thesis, Heriot-Watt University, 2017.

[85] G. Juzeliūnas, P. Öhberg, J. Ruseckas, and A. Klein, Effective magnetic fields in degenerate atomic gases induced by light beams with orbital angular momenta, Phys. Rev. A **71**, 053614 (2005).

[86] K. Enomoto, K. Kasa, M. Kitagawa, and Y. Takahashi, Optical Feshbach Resonance Using the Intercombination Transition, Phys. Rev. Lett. **101**, 203201 (2008).

[87] M. N. Tengstrand, P. Stürmer, E. Ö. Karabulut, and S. M. Reimann, Rotating Binary Bose-Einstein Condensates and Vortex Clusters in Quantum Droplets, Phys. Rev. Lett. **123**, 160405 (2019).

[88] S. Xie, P. G. Kevrekidis, and T. Kolokolnikov, Multi-vortex crystal lattices in Bose-Einstein condensates with a rotating trap, Proc. R. Soc. A **474**, 2213 (2018).

[89] S. K. Adhikari, Vortex-lattice in a uniform Bose-Einstein condensate in a box trap, J. Phys.: Condens. Matter **31**, 275401 (2019).

[90] R. Doran and T. P. Billam, Numerical method for the projected Gross-Pitaevskii equation in an infinite rotating two-dimensional Bose gas, Phys. Rev. E **102**, 033309 (2020).

[91] C. Barenghi and N. G. Parker, *A Primer on Quantum Fluids* (Springer, Berlin, 2016).

[92] M. Correggi, R. Duboscq, D. Lundholm, and N. Rougerie, Vortex patterns in the almost-bosonic anyon gas, Europhys. Lett. **126**, 20005 (2019).

[93] B. T. Seaman, M. Krämer, D. Z. Anderson, and M. J. Holland, Atomtronics: Ultracold-atom analogs of electronic devices, Phys. Rev. A **75**, 023615 (2007).

[94] S. Eckel, J. G. Lee, F. Jendrzejewski, N. Murray, C. W. Clark, C. J. Lobb, W. D. Phillips, M. Edwards, and G. K. Campbell, Hysteresis in a quantized superfluid 'atomtronic' circuit, Nature (London) **506**, 200 (2014).